Modeling of oxygen gas diffusion and consumption during the oxic transient in a disposal cell of radioactive waste

Laurent de Windt, François Marsal, Jérôme Corvisier, Delphine Pellegrini

Modeling of oxygen gas diffusion and consumption during the oxic transient in a disposal cell of radioactive waste

Laurent De Windt[1,*], François Marsal[2], Jérôme Corvisier[1], Delphine Pellegrini[2]

[1]Mines-ParisTech, Centre de Géosciences, 77305 Fontainebleau cedex, France
[2]IRSN, PRP-DGE/SEDRAN/BERIS, B.P. 17, 92262 Fontenay-aux-Roses Cedex, France

* *Corresponding author, Email = laurent.dewindt@mines-paristech.fr*
Tel = +33-1-64.69.49.42 ; Fax = +33-1-64.69.47.13

Abstract.

The oxic transient in geological radioactive waste disposals is a key issue for the performance of metallic components that may undergo high corrosion rates under such conditions. A previous study carried out in-situ in the argillite formation of Tournemire (France) has suggested that oxic conditions could have lasted several years. In this study, a multiphase reactive transport model is performed with the code HYTEC to analyze the balance between the kinetics of pyrite oxidative dissolution, the kinetics of carbon steel corrosion and oxygen gas diffusion when carbon steel components are emplaced in the geological medium. Two cases were modeled: firstly, the observations made in-situ have been reproduced, and the model established was then applied to a disposal cell for high-level waste (HLW) in an argillaceous formation, taking into account carbon steel components and excavated damaged zones (EDZ).
In a closed system, modeling leads to a complete and fast consumption of oxygen in both cases. Modeling results are more consistent with the in-situ test while considering residual voids between materials and/or a water unsaturated state allowing for oxygen gas diffusion (open conditions). Under similar open conditions and considering ventilation of the handling drifts, a redox contrast occurs between reducing conditions at the back of the disposal cell (with anoxic corrosion of steel and H_2 production) and oxidizing conditions at the front of the cell (with oxic corrosion of steel). The extent of the oxidizing/reducing front in the disposal cell is strongly dependent on the gas diffusion coefficient in partially saturated zones.

Keywords: multiphase, oxic stage, reactive transport, redox, steel corrosion.

1. Introduction

The environment in a deep geological disposal of high-level radioactive waste (HLW) will be initially aerated, due to the air introduced into the disposal cell during its excavation and waste emplacement. The project developed in France by Andra involves carbon steel materials and horizontal disposal cells in Callovo-Oxfordian argillite, containing significant amounts of pyrite. The oxygen is considered initially entrapped in the porosity of materials and in the residual voids between components. In addition, it is assumed that the ventilation of handling drifts will renew oxygen at the front of the disposal cell over a period from a few years to many decades. So far, the reducing conditions generally prevailing in deep geological environments are supposed to be quickly restored after the closure of such facilities because of the consumption of the oxygen by corrosion of the carbon steel (C-steel) of waste overpacks, oxidation of pyrite of the host rock and, to a probably lesser extent, microbial activities (e.g. Wersin et al., 2003; Yang et al., 2007; Bennett and Gens, 2008; Johnson and King, 2008). However, the duration of this oxic stage is of first importance since corrosion rates under oxic conditions are known to be particularly high (Féron et al., 2008; Johnson and King, 2008) and may thus lead to a premature loss of the watertightness of metallic components, as well as an alteration of their mechanical integrity.

A previous study of the in-situ corrosion of carbon steel samples was carried out in boreholes drilled horizontally in the Tournemire experimental site (France), a century-old tunnel crossing a 250 m thick formation of Toarcian argillite (a fine-grained sedimentary rock composed predominantly of indurated clay particles). The steel samples were representative of carbon steel overpacks that may be selected for radioactive waste geological disposal. The tunnel was naturally ventilated. The experimental concept, the materials and the results have been detailed by Foct et al. (2004) and Gaudin et al. (2008). C-steel samples (A42 type) were placed in a 10 m long borehole filled in by re-compacted argillite, during 6 years, at 8 m from the wall of the tunnel. The re-compacted argillite materials used for this experiment indicated a near isotropic texture. The analytical characterization of the sample interface showed a Fe-rich enrichment of the altered argillite, concomitant with the crystallization of significant amounts of goethite/lepidocrocite and some traces of magnetite near the C-steel contact. The crystallization of few amounts of gypsum and melanterite, probably due to pyrite oxidation, was also noted. Dissolution of primary calcite minerals and calcium leaching was also revealed, probably related to a slight decrease of pH due to pyrite oxidation. Eventually, localized corrosion patterns were highlighted on the C-steel coupons. Although oxygen partial pressure was not monitored during the 6 years of interaction, these observations led to the conclusion that oxidizing conditions had lasted a significant period of time, even though the presence of magnetite tends to show that reducing conditions were recovered before the end of this period. This indicates that usual assumptions, such as fast oxygen consumption by pyrite, have to be partly reconsidered in the case of open conditions such as an open ventilated tunnel scenario.

From a modeling point of view, to the authors' knowledge, there are only a few studies devoted to the consumption of oxygen entrapped in the voids of the near-field components and to the short-term geochemical evolution during this oxic stage in a HLW repository (Kolar and King, 1996; Yang et al., 2007; the technical reports of Wersin et al., 1994 and Wersin et al., 2003). These previous studies have considered, neither the reactive transport of oxygen in the gas phase, nor the extension of the oxidizing perturbation inside the whole disposal cell in case of ventilation.

In a preliminary step, this study aims at deciphering the physico-chemical processes involved in the oxygen consumption in the Tournemire in-situ experiment. For this purpose, a reactive transport model was developed, which included gas diffusion, aqueous chemistry, cation exchange and dissolution/precipitation processes. Kinetic formulations were introduced for C-steel corrosion and pyrite dissolution under both oxic and anoxic conditions, as well as an empirical relationship between the gas diffusion coefficient and the water saturation.

In the core of the present work, the resulting model was then applied to the 2D-configuration of a HLW disposal cell in a deep argillaceous formation representative of the design developed in France by Andra (Andra, 2005). The main point was to assess the extent of the oxic perturbation

inside the cell when the ventilation is maintained in the handling drift, and to model the redox contrast between the back and the front of the disposal cell. Simulations were performed over a 100 y timescale, which is the estimated period of the operation phase for a HLW disposal before its closure. Temperature was set to 25 °C, which underestimates the temperature of the environment of HLW disposal cells during this period, estimated between 50 and 90 °C (Andra, 2005). However, modeling of interdependent and coupling effects of heat transfer, gas phase physics, vapor evaporation/condensation, water resaturation of the porous components, C-steel corrosion and chemical reactions is a highly complex task that cannot be be handled by the code. This paper considers a subset of those processes, i.e. gas diffusion and reactivity (for both H_2 and O_2), C-steel corrosion, redox chemistry and pH-buffering.

2. Modeling approach and parameters

2.1. HYTEC reactive transport code

The reactive transport code HYTEC is based on a finite element discretization in a representative elementary volume (REV) approach and a sequential iterative operator-splitting method for coupling between chemistry and transport (van der Lee et al., 2003). A simplified two phase dynamics of mass transfer can be simulated, namely a reactive transport modeling in the water phase linked to diffusion in the gas phase.

Under water unsaturated conditions, the general HYTEC formulation of the reactive transport of solute writes as follows:

$$\frac{\partial\left(\theta^w T_i^w\right)}{\partial t} = \nabla\cdot\left(D_e^w\left(\theta^w\right)\nabla T_i^w\right) + Q_i^w \qquad \text{(Eq. 1)}$$

where θ^w is the volumetric content of the water phase, T_i^w is the total aqueous concentration of an element or basis component *i* per unit volume of solution [mol.L^{-1}], D_e^w is the effective diffusion coefficient in the aqueous phase common to all elements [m^2.s^{-1}] and Q_i^w is the source-sink term of the element *i* [mol.L^{-1}.s^{-1}] driven by the chemical reactions with the gas and solid phases. D_e^w is itself a function of the water content according to the relation:

$$D_e^w\left(\theta^w\right) = \frac{\theta^w}{\omega} D_{e,sat}^w = S^w D_{e,sat}^w \qquad \text{(Eq. 2)}$$

where ω is the total porosity of the porous media, S^w is the water saturation degree and $D_{e,sat}^w$ is the effective diffusion coefficients [m^2.s^{-1}] at water fully saturated conditions.

The reactive transport equation for the gaseous phase writes as

$$\frac{\partial\left(\theta^g C_j\right)}{\partial t} = \nabla\cdot\left(D_e^g(\theta^g)\nabla C_j\right) + Q_j^g \qquad \text{(Eq. 3)}$$

where θ^g is the volumetric content of the gas phase, C_j is the concentration of a gas species *j* regarding the gas phase volume [mol.L^{-1}], D_e^g is the effective diffusion coefficient in the gas phase common to all gas molecules [m^2.s^{-1}] and Q_j^g is linked to the variation of the partial pressure of the gas species *j* [(mol.L^{-1}).(sec^{-1})] driven by the dissolution of the gas in the aqueous phase according to the Henry's law.

In this study, the empirical relationship of Aachib et al. (2004) was selected to estimate the dependency of D_e^g on θ^g (i.e. indirectly with the water saturation state since $\theta^g = \omega - \theta^w$). That writes as:

$$D_e^g\left(\theta^g\right) = \frac{\left(\theta^g\right)^{3.3}}{\omega^2} D_o^g \ , \qquad \text{(Eq. 4)}$$

where D_o^g is the gas diffusion coefficient in air. This law has been calibrated for oxygen gas diffusion in unsaturated media with applications to soil cover. It has recently been applied to numerical simulations of pyrite oxidation in unsaturated waste rock piles (Molson et al., 2005).

The concentration of each gas species is related to its partial pressure according to the perfect gas law, which was a good approximation under the pressure (~1 bar) and temperature (25 °C) of the present study. That is to say

$$C_j = \frac{p_j}{RT} \qquad \text{(Eq. 5)}$$

where n is the number of mole, T is the absolute temperature [K] and R is the perfect gas constant [L.bar.K^{-1}.mol^{-1}]. The Dalton's law is, therefore, applicable: (Eq. 6)

$$P = \sum_j x_j \, p_j \qquad \text{(Eq. 6)}$$

where P is the total pressure of the gas phase [bar] and x_j is the mole fraction of the species j.

The mass balance is made over the aqueous (dissolved) phase, the solid phases (including the mineral and fixed fractions) and eventually the gas phase:

$$T_i^{tot} = T_i^w + T_i^s + T_i^g \qquad \text{(Eq. 7)}$$

The corresponding sum of the subtotal concentrations is expressed in terms of mole per kg of water, of which the gas contribution is calculated according to the following expression:

$$T_i^g = \left(\frac{p_i \theta^g}{RT}\right)\left(\frac{1}{\theta^w \rho_{H_2O}}\right) \qquad \text{(Eq. 8)}$$

where ρ_{H_2O} is the water density [kg.L^{-1}] at the given temperature (25 °C in this study).

2.2. Modeling scenarios and two-phase transfer parameters

Two sets of simulations were performed: the first one reproduced the observations made on the Tournemire in-situ experiment, the second one applied this model to a HLW disposal cell. The Toarcian argillite of Tournemire was considered in both cases, given its chemical and physical properties close to those of Callovo-Oxfordian argillite studied in France to host a HLW disposal facility.

Two modeling scenarios were considered according to the degree of water saturation and the voids between the cell components. The scenario 1 assumes that, during the simulated duration (100 years):

- residual voids between re-compacted argillite and host rock in the Tournemire borehole on the one hand, and between C-steel liner and argillite host rock in the HLW disposal cell on the other hand, allow for air diffusion;
- the initial water saturation state does not evolve;
- the Tournemire tunnel and the handling drift, to which many disposal cells are connected, are constantly ventilated with air (open system). This is associated to the stepwise closure or "reversibility phase" of the HLW repository. In a variant (so-called scenario 1b) the Tournemire borehole and the disposal cell are not submitted to air ventilation (closed system).

The scenario 2 represents an intermediate stage between scenario 1 and a full resaturation state with perfect contacts between all the materials. Table 1 provides the physical parameters assigned to each components of the Tournemire borehole and the disposal cell as a function of the scenario. The diffusion parameter of the undisturbed argillite corresponds to the mean value of samples collected at the same stratigraphical level as the borehole at Tournemire (Motellier et al., 2007). Fissured and fractured EDZ with higher diffusion coefficients were also taken into account

in the calculations. The fractured EDZ in indurated clayey rocks present (sub)millimetric interconnected cracks (Charpentier et al. 2001; Bossart et al., 2002; Matray et al., 2007). These cracks were assumed to be fully desaturated, leading to the low water saturation degrees of these zone (Table 1) in the present elementary volume representation (that averages matrix and crack properties). The same approach was followed for the voids that could remain inside the recompacted argillite of the Tournemire in-situ experiment.

[TABLE 1]

2.3. Geochemical modeling and parameters

All the chemical reactions were calculated under thermodynamic equilibrium, except for the dissolution/precipitation of pyrite and the corrosion of C-steel that were under kinetic constraints (Sec. 2.4). Stoichiometric coefficients and thermodynamic equilibrium constants for minerals and aqueous species were taken from the EQ3/6 database (Wolery, 1992), though only a subset of data was selected for the dissolved redox species, gas and minerals, as reported in Table 2. Hydrogen was decoupled from redox reactions to avoid hydrogen reaction with oxygen and sulfates, which is thermodynamically possible but kinetically hindered at low temperature.

The main goal of this paper is the extension of the oxidizing front inside the disposal cell, which results from two opposite forces: i) kinetics of oxygen consumption by pyrite and steel and ii) oxygen gas diffusion. The formation of corrosion products is of secondary importance. Calcite dissolution and gypsum reaction are known to be fast reactions. Therefore, a thermodynamic equilibrium approach for secondary minerals was a reasonable choice. Similarly, the calculation of the exact amounts of precipitated masses that may depend on grid size (Marty et al., 2009) by imposing the equilibrium constraint was not a central issue of the paper.

In this paper, emphasis was put on the competition between the kinetics of iron and pyrite oxidation at a relatively short timescale. Accordingly, the cation exchangeable populations and the mineralogy of the Tournemire argillite (Deniau et al., 2008; Gaudin et al., 2009) and of the MX80 bentonite (Wersin, 2003) were simplified. Table 3 details the reactions and parameters selected for cation exchange and surface complexation modeling. The mineral phases of the argillite and bentonite (37.5 wt% and 95 wt% respectively) were assumed to be only active through their cation exchange and surface complexation properties without any potential (slow) dissolution processes. The bentonite has a much higher cation exchange capacity (CEC = 75 meq/100g) than the argillite (CEC = 15 meq/100g), though the lower CEC of the argillite is partly compensated by its higher bulk density. Calcium is the main exchangeable cation of the argillite (Ca = 0.73, Na = 0.27, equivalent fractions), whereas sodium is the predominant exchangeable cation of the MX80 bentonite (Na = 0.85, Ca = 0.15, equivalent fractions). In addition to cation exchange of clayey phases, a set of reactive minerals was considered for the argillite (calcite, 20 wt%; pyrite, 1.5 wt%; quartz, 41 wt%) and the bentonite (calcite, 1.5 wt%; quartz, 3.5 wt%). C-steel was assumed to consist of pure metallic iron (Fe(s), 100 wt%). Goethite, gypsum, magnetite, melanterite and siderite were considered as secondary mineral phases that could also precipitate in the calculations.

In the water unsatured zones the partial pressure of oxygen in the gas phase was initially fixed to 0.21 bar in equilibrium with the aqueous phase, whose dissolved oxygen concentration was 2.5×10^{-4} mol.L^{-1}. These zones were therefore initially under oxidizing conditions (redox potential Eh = 0.765 V at pH = 7.5). In the fully saturated argillites, there was no entrapped oxygen and the porewater were initially under reducing conditions controlled by pyrite and the aqueous sulfate concentration (Eh = -0.200 V at pH = 7.0).
The introduction of microbial species during the construction and operational phases of the disposal nor the survival of bacteria after its closure cannot be excluded (Chautard et al., 2012). Microbial activity can affect both oxygen consumption by respiration under oxic conditions and hydrogen consumption coupled to sulfate reduction under anoxic conditions. However, these activities are still poorly known from a quantitative point of view in the present indurated clay rock that present very low porosity and water content. These processes were therefore skipped

from the present modeling to better clarify the interdependency of inorganic reactions (corrosion, oxidation) and gas diffusion.

[TABLES 2 & 3]

2.4. Kinetics of pyrite oxidation

Two main processes consuming oxygen were considered in the modeling: i) the oxic corrosion of C-steel materials (Sec. 2.5) and ii) the oxidation of pyrite in the EDZ and the argillite (this section). Organic matter of sedimentary origin is present in the argillite of Tournemire, but at a low content (< 1 wt%) and under the form of matured kerogens (Deniau et al., 2008). Its reactivity with oxygen is therefore unlikely at 25 °C. The argillite has also a minor content in chlorite (Gaudin et al., 2009), a Fe(II)-clay phase that may react with oxygen. However, the kinetic constant of chlorite dissolution is relatively low (~10^{-13} mol.m^{-2}.s^{-1} at 25°C and circumneutral pH; Lowson et al., 2005) compared with the constant of pyrite oxidative dissolution (~10^{-10} mol.m^{-2}.s^{-1} under the same conditions and p_{O2} = 0.21 bar, see below). Actually, there are several field observations that point out the predominant reactivity of pyrite under oxic environments in tunnels and galleries excavated in argillaceous formations (e.g. Charpentier et al., 2001; De Craen et al., 2008).

In the presence of oxygen, pyrite oxidation is driven by the following global reaction:

$$pyrite + \tfrac{15}{4}\, O_2(aq) + \tfrac{5}{2}\, H_2O \rightarrow goethite + 2\, SO_4^{2-} + 4\, H^+ \qquad \text{(Eq. 9)}$$

Under anoxic conditions, pyrite is subjected to dissolution/precipitation reactions such as:

$$pyrite + H_2O \leftrightarrow Fe^{2+} + \frac{7}{4} HS^- + \frac{1}{4} SO_4^{2-} + \frac{1}{4} H^+ \qquad \text{(Eq. 10)}$$

The following general kinetic equation was used to simulate pyrite dissolution under oxic (*ox*) conditions (irreversible reaction) and dissolution/precipitation under anoxic (*anox*) conditions (reversible reaction, with forward and backward rates):

$$\frac{d[FeS_2]}{dt} = A_v\, f_{Sw} \left(-k_{ox} \left(O_2(aq)\right)^{0.5} + k_{anox} \left(\frac{Q_i}{K_i^{-1}} - 1 \right) \right) \qquad \text{(Eq. 11)}$$

where the brackets stand for the Fe molal concentration in the solid, A_v is the surface area per volume of solution [m^2.L^{-1}], f_{Sw} is a water saturation factor, k_{ox} and k_{anox} are the intrinsic rate constants under oxic and anoxic conditions [mol.m^{-2}.s^{-1}], $O_2(aq)$ is the activity of dissolved oxygen. The term $\left(\frac{Q_i}{K_i^{-1}} - 1 \right)$ is the saturation state where Q_i stands for the ion activity product and K_i is the thermodynamic formation constant. While approaching equilibrium, this term converges towards zero likewise the kinetic rate.

The kinetic parameters used for this study are reported in Table 4. The square-root dependency with respect to dissolved oxygen is commonly found in the literature about the oxidative dissolution of pyrite. The rate constants k'_{ox} may vary over one order of magnitude: from 5×10^{-8} mol.m^{-2}.s^{-1} (Williamson and Rimstidt, 1994) to 5×10^{-9} mol.m^{-2}.s^{-1} (Moses and Herman, 1991; Domènech et al., 2002) at 25 °C and circumneutral pH. In the present study, the latter value (5×10^{-9} mol.m^{-2}.s^{-1}) was selected as the base-case, and the former and higher constant for the sake of sensitivity analysis. The rate constant k_{anox} of pyrite dissolution under anoxic conditions (k_{anox} = 10^{-16} mol.m^{-2}.s^{-1}) came from the modeling study of Marty et al. (2010).

The anoxic constant is several orders of magnitude lower than the oxic one. This significant difference and the implementation of Eq. 11 as a sum of the oxic and anoxic terms allow the code to automatically and smoothly shift from a rate type to the other. For instance, in a mesh in which in equilibrium with the atmosphere is supposed, the oxic term $k'_{ox}(O_2^{init}(aq))^{0.5}$ is equal to 8×10^{-11} mol.m^{-2}.s^{-1} and the effect of the additional anoxic term to the rate law is negligible. If the redox

state becomes locally anoxic during the calculations, the oxygen concentration will drop to zero as well as the oxic term. The anoxic term will then become predominant.

The surface area A_v is usually derived from the specific surface of the mineral A_s. The specific surface of pyrite crystals given in the literature ranges from 0.01 to 10 $m^2.g^{-1}$. The lowest value corresponds to cubic pyrite crystals whereas the highest value corresponds to framboidal pyrites. Both morphologies occur in Tournemire: cubic crystals are present in fractures and veins whereas the framboidal shape is ubiquitous in the argillites matrix (Mathieu et al., 2000). Furthermore, the surface effectively available for reaction once the crystals are embedded in the matrix is lower than the surface measured on isolated specimens. An intermediate value of 0.1 $m^2.g^{-1}$ was taken into account as a compromise between both a low accessibility of pyrite in the argillite matrix and a good representativeness of the Tournemire argillite.

Some influence of the water saturation degree (S^w, Eq. 2) on the corrosion rate was also taken into account for the mostly desaturated zones of the modeling grid; i.e. the pyrite within the fractured EDZ in the water-saturation scenario 1. This dependency is still unclear in the literature. Oxygen consumption measurements in unsaturated waste rock piles demonstrated that the rate of pyrite oxidation was strongly dependent on grain size (i.e. specific surface) but moderately to slightly on water content (Hollings et al., 2004). However, the lowest rates were found for the smallest water contents. Jerz and Rimstidt (2004) experimentally found that the rate of pyrite oxidation in moist air was higher than the aqueous oxidation rate at very short reaction times but became rapidly slower. For the sake of consistency, the same reducing factor (f_{Sw} = 0.2, factor 5) as steel corrosion was applied (see below).

[TABLE 4]

2.5. Kinetics of carbon steel corrosion

Under oxic conditions, metallic iron Fe(0) is not stable and reacts with oxygen to form Fe(III)-corrosion products such as goethite:

$$Fe(s) + \tfrac{3}{4}\, O_2(aq) + \tfrac{1}{2}\, H_2O \rightarrow goethite \qquad \text{(Eq. 12)}$$

Once oxygen is fully depleted, metallic iron is corroded by water under reducing conditions to form corrosion products like magnetite as well as molecular hydrogen:

$$3Fe(s) + 4H_2O \rightarrow magnetite + 4H_2(aq) \qquad \text{(Eq. 13)}$$

Melanterite, pyrite and siderite are the other Fe(II)-corrosion products that could precipitate in the calculations.

From a review of the literature, Féron and co-authors (2008) have proposed two empirical laws for the general (uniform) corrosion of C-steel under oxic and anoxic conditions. The rate constants are expressed in terms of corroded thickness per year. The mean oxic and anoxic rates at 25 °C are 12 $\mu m.y^{-1}$ and 2 $\mu m.y^{-1}$, respectively. Furthermore, the additional effect of pitting corrosion can be significant during the first years of C-steel corrosion under oxic conditions. Corrosion depths of hundreds of microns have been measured on the C-steel samples placed in a similar Tournemire in-situ experiment during 2 years (Foct et al., 2004). In the present study, general and pitting corrosions were not differentiated and a maximized rate of 100 $\mu m.y^{-1}$ under oxic conditions has been set in the base-case calculations. This is a penalizing approach since pitting corrosion is one of the most aggressive forms of corrosion. The possibility of such a localized corrosion of C-steel during the early aerated phase has also been considered in several performance assessments of HLW disposals (JNC, 2000; NAGRA, 2002; Johnson and King, 2008). A complementary calculation without pitting corrosion (corresponding to a rate of 10 $\mu m.y^{-1}$) was made in complement for the sake of sensitivity analysis.

To keep benefit of the computational method for shifting from an oxic rate law to an anoxic rate law (and conversely), the formalism of Eq. 11 was also applied to the modeling of iron corrosion

since the anoxic rate constant is also numerically negligible with respect to the oxic rate constant. The combination of these two irreversible laws (metallic iron cannot be formed in a backward scheme) writes as:

$$\frac{d[Fe(s)]}{dt} = A_v\, f_{Sw} \left(-k_{ox} \left(O_2(aq) \right)^{0.5} - k_{anox} \right) \qquad \text{(Eq. 14)}$$

Some influence of the water saturation degree (S^w, Eq. 2) on the corrosion rate was also taken into account: the atmospheric corrosion rate of iron decreases by one order of magnitude when the relative humidity goes from 100 % to 50 % (Ben Lagha et al., 2007). Similarly, the aqueous corrosion rate was reduced by a factor 5 (i.e. f_{Sw} = 0.2 in Eq. 11) for the mostly desaturated zones of the modeling grid: the fractured EDZ and the C-steel lining in the water-saturation scenario 1.

The calculated specific surface of the lining ($A_s \sim 2\times10^{-6}$ $m^2.g^{-1}$) was based on the lining external diameter and the mass of both lining and overpack (see the beginning of Sec. 4). Owing to the lack of relevant data, that specific surface did not take into account any surface roughness and, therefore, constituted a lower limit with respect to the kinetics of C-steel corrosion.

3. Tournemire borehole: oxygen diffusion and oxidizing plume

The 2D-cylindrical grid used to model the Tournemire in-situ experiment is given in Fig. 1. The diameter and length of the borehole are 45 mm and 10 m, respectively. The borehole damaged zone (BDZ) within the argillite is estimated about 10 mm thick. The influence of the gallery is taken into account through boundary conditions where the gas partial pressures are constant and set to their atmospheric values (p_{O2} = 0.21 bar, $p_{CO2} = 4\times10^{-4}$ bar, $p_{H2} = p_{H2S}$ = 0 bar).

As shown in Fig. 2A, the complete consumption of the gaseous and dissolved oxygen, initially entrapped in the re-compacted argillite and the BDZ, requires 60 days in the base-case scenario 1b (no water resaturation but a closed system without any air exchanges). The duration for the full oxygen consumption once the pyrite oxidation rate is increased by a factor 10 drops to 12 days approximately. Oxygen content and redox potential reach a steady state within a few months while considering the scenario 2 (advanced but not complete saturation state and open connection between the gallery and the borehole). Nevertheless, the gaseous oxygen that diffuses inside the borehole is consumed over the first meter and the extension of the oxidizing plume remains restricted to the proximity of the gallery (Fig. 3). At the back of the borehole, the redox potential inside the re-compacted argillite is about -80 mV and the pH is around 7. Such redox conditions are reducing but less than those prevailing in the undisturbed argillite (-200 mV, for a similar pH). Neither oxic C-steel corrosion, nor pyrite dissolution, nor goethite precipitation occur deep inside the borehole. Therefore, results obtained with both scenario 1b and 2 are not consistent with the observations made on the C-steel samples located at the back of the borehole (see Introduction and Gaudin et al., 2008).

In scenario 1, oxygen content and redox potential also reach a steady state within a few months (Fig. 3). However, in that case, the oxidizing plume covers the whole borehole. The redox potential Eh stays above 750 mV and the pH is buffered around 7 inside the re-compacted argillite and the BDZ. These modeling results are closer to the observations than those obtained with scenario 1b and 2: oxic corrosion of C-steel and pyrite oxidation inside the BDZ occur due to a permanent diffusion of oxygen over the whole length of the borehole, leading to goethite precipitation, calcite dissolution and gypsum precipitation. Furthermore, Foct et al. (2004) pointed out that some macroscopic cavities were observed inside the recompacted argillite and that these cavities were not filled by water after 2 years. This tends to confirm that resaturation was not complete at that time with probable presence of oxygen deep in the borehole.
The mineralogical evolution is not detailed in this section, but is further discussed in the case of a HLW cell in Sec. 4.2. This supports the hypothesis made in scenario 1, considering residual voids and/or an imperfect BDZ/filling interface under permanent unsaturated conditions. However, the model in this scenario does predict magnetite precipitation, which has been observed at a

micrometer scale in contact with steel surfaces in the in-situ experiment. The paragenesis goethite/magnetite indicate that either reducing conditions were recovered at the end of the experiment, or reducing conditions can occur very locally around the steel samples.

[FIGURES 1, 2 & 3]

4. HLW disposal cell: gas diffusion, oxidizing plume and mineralogy evolution

The configuration of the HLW disposal cell was modeled in a 2D-cylindrical geometry (Fig. 4). The cell radius is about 30 cm. The head of the cell (first 8 meters) is sealed with bentonite (7.5 m) and C-steel (0.5 m), whereas the useful part of the cell (12 m) contains the waste packages. In disposal concepts the length of useful part of the cell can be as high as 40 m but the considered first 12 m are representative of the global processes. This useful part is composed, from the outer to the inner, by a C-steel liner (2.5 cm thick) and a C-steel overpack (7.5 cm thick), which are merged in a single component (10 cm thick) for the sake of simplicity. The vitrified wastes are not explicitly considered in the modeling grid. The EDZ of the cell is split into a fractured zone (10 cm thick) and a fissured zone (25 cm thick). The fractured EDZ is considered in contact with the liner without an explicit representation of the interstices and imperfect contacts by grid nodes. However, the effect of such heterogeneities is taken into account through the ability of gas to diffuse in the unsaturated zones along the lining. The influence of the handling drift is taken into account through boundary conditions considering constant gas partial pressures over time (atmospheric values, p_{O2} = 0.21 bar, $p_{CO2} = 4\times10^{-4}$ bar and $p_{H2} = p_{H2S}$ = 0 bar). The EDZ of the handling drift is also taken into account, this EDZ being also split into a fractured zone (0.5 m thick) and a fissured zone (1.5 m thick).

[FIGURE 4]

4.1. Diffusion of oxygen gas and extension of the oxidizing plume

As shown in Fig. 2B, the full consumption of the gaseous and dissolved oxygen, initially entrapped in the voids around the liner as well as in the EDZ and bentonite seal of the cell, requires about 80 days in scenario 1b (initially unsaturated conditions but closed system, i.e. no gas exchange with the handling drift). Previous performance assessment calculations of a spent fuel disposal also led to the conclusion of a short oxic transient stage under such closed conditions (Wersin et al., 2003). The sensitivity analysis indicates that this duration is shortened to 10 days if the pyrite oxidation rate is increased by one order of magnitude. That is to say that the global oxygen consumption is (inversely) proportional to the rate constant of pyrite oxidation. On the contrary decreasing the rate constant of oxic steel corrosion by one order of magnitude (i.e. suppressing the pitting factor) has a weaker impact on the global consumption of oxygen in the cell. The duration of the oxic transient rises from 80 to 95 days only. Globally pyrite reactivity seems to predominate over steel reactivity in the present system.

In scenario 1 (open voids and water unsaturated conditions promoting air diffusion from the ventilated handling drift), the profiles of oxygen content and redox potential reach steady-state in less than 6 months approximately. The diffusion of oxygen gas takes place over the whole disposal cell as well as inside the fissured and fractured EDZ (Fig. 5), though more than 95 % of the oxygen is consumed while reaching the back of the cell. The penetration of oxygen also occurs in the fractured EDZ of the handling drift and, to a lesser extent, in the fissured EDZ. There is no oxygen diffusion inside the undisturbed argillite which is fully water saturated. Consequently, the EDZ and the lining zones are entirely under oxidizing conditions (redox potential Eh > 800 mV at circumneutral pH, Fig. 5). On the contrary, the argillite constantly remains under reducing conditions (Eh ≤ -200 mV at circumneutral pH). Experimentally, the in-situ ventilation test performed in the HADES underground laboratory (Belgium) has shown that the extent of the oxidizing plume within the Boom Clay was only related to the fractured zone of the EDZ of the gallery without perturbation of the undisturbed rock (De Craen et al., 2008).

The situation is significantly different in scenario 2 considering perfect interfaces between materials. Only the 5 five meters of the disposal cell are disturbed by the oxidizing plume (Eh > 800 mV at circumneutral pH, Fig. 5), mostly inside the fractured EDZ and the bentonite seal. There are no oxygen-consuming minerals in the latter, but the fast oxygen diffusion in the gas phase allows its consumption by pyrite in the adjacent fractured EDZ. The fissured EDZ of the gallery, and to a lesser extent of the cell, are not affected by oxygen and remain under reducing conditions (Eh ≤ -200 mV at circumneutral pH). The HLW packages are constantly under reducing conditions too. The redox conditions (Eh = -250 mV at circumneutral pH) are more reducing than those of the pristine argillite because the anoxic corrosion of C-steel liberates Fe(II) ions in water. The solubility of Fe(II) is, however, controlled by magnetite precipitation (Sec. 4.2). The redox potential would even be more reducing (Eh ~ -500 mV) if hydrogen was considered as an active redox species in the calculations.

The main reason for the lesser penetration of oxygen in scenario 2 compared to scenario 1 is the decrease of the effective diffusion coefficient of gas, as reported in the last column of Table 1. Along the fractured EDZ of the cell and the gallery, which are the most preferential migration paths in the modeling, the effective coefficient of oxygen gas diffusion is reduced by a factor 25 (D_e^g decreasing from 1.5×10^{-6} $m^2.s^{-1}$ to 6.5×10^{-8} $m^2.s^{-1}$). There is no oxygen gas diffusion inside the fissured EDZ of the cell and the gallery that are fully water saturated in scenario 2. Oxygen penetration in these zones is driven by the slow aqueous diffusion of dissolved oxygen only ($D_{e,sat}^w = 1.5\times10^{-11}$ $m^2.s^{-1}$); this dissolved oxygen is easily depleted by the reaction with pyrite. A secondary parameter explaining that oxygen penetration is reduced in scenario 2 is that kinetic rates of pyrite and C-steel oxidation inside the fractured EDZ is increased by a factor 5 due to the higher water content (factor f_{Sw} is equal to 1 in Eq. 11).

The sensitivity analysis on Eh profiles (Fig. 6) indicates that the global conclusions drawn above are not changed while the rate constant of pyrite oxidation becomes 10 times higher. The oxic front penetrates inside the cell up to the waste disposal zone in scenario 1 (though to a lesser extent than in the base case) whereas it remains localized to the cell entrance in scenario 2.

[FIGURES 5 & 6]

4.2. Mineralogical reactions and C-steel corrosion

The diffusion of oxygen gas is the driving force of the mineralogical transformations since, once dissolved, molecular oxygen can react with pyrite and yields goethite precipitation according to Eq. 9. The overall process also releases protons in water. However, that acidic plume is efficiently buffered by calcite dissolution (as a result the pH decreases by 0.4 pH units to the maximum):

$$calcite + H^+ \rightarrow Ca^{2+} + HCO_3^- \qquad \text{(Eq. 15)}$$

The contribution of the surface hydroxyl groups of the clayey phases (S_1-OH and S_2-OH, Table 4) to pH buffering is of minor importance in this modeling. The dissolved Ca^{2+} ions combine with aqueous sulfates to eventually lead to gypsum precipitation:

$$Ca^{2+} + SO_4^{2-} + H_2O \rightarrow gypsum \qquad \text{(Eq. 16)}$$

The sulfates come from pyrite oxidation and, to a much lesser extent, from the diffusion of the sulfates naturally present in the porewater of the argillite. Independently from pyrite oxidation, there is a slow exchange process (not shown) between the exchangeable sodium of the MX80 bentonite and the exchangeable calcium of the argillite. Such a redistribution of the exchangeable population is not affected by the (relatively weak) additional input of calcium brought by pyrite oxidation and the subsequent calcite dissolution.

As shown in Fig. 7, there is an anti-correlation between the pyrite content (that decreases with time) and the gypsum content (that increases with time) in agreement with the reaction scheme of

Eqs. 9, 15 and 16. That mineralogical trend is especially exacerbated in the fractured EDZ (of the cell and the gallery) in scenario 1, as shown in Fig. 7. In close relation with the dissolved oxygen profile of Fig. 5, the back of the disposal cell is partly protected from the mineralogical effects of oxygen intrusion by the upstream zones (i.e. the handling drift and the disposal cell front). This protection is even complete in scenario 2. After 100 years, the pyrite content in the most reactive zones of the fractured EDZ has dropped by 50 % in both scenarios. However, the extension of this chemically disturbed zone remains very localized over the first 2 meters of the disposal cell in scenario 2.

In scenario 1, goethite formation takes place over the whole length of the EDZ of the cell similarly to gypsum precipitation both in the fissured and fractured EDZ (Fig. 7). There is a clear contribution of C-steel corrosion in addition to pyrite oxidation, in particular from the C-steel seal and the first meters of the lining that are more corroded than the lining at the back of the cell (Fig. 7 and Fig. 8A). In scenario 1, the analysis of the goethite profile indicates that the overall rate of oxygen consumption is approximately 5 times higher (faster) in the case of C-steel corrosion than pyrite oxidation. The predominance of steel corrosion vs. pyrite oxidation is for a large part related to the maximized approach that integrates both pitting and general corrosion in a single rate (Sec. 2.5). Nevertheless, since pyrite is more widespread in the system than the C-steel components, the contribution of pyrite is globally predominant (as already pointed out in the discussion on the closed system configuration).

In scenario 2, the precipitation of goethite is restricted to the first meters of the EDZ of the disposal cell as well as gypsum precipitation (Fig. 7). As observed in scenario 1, both the fissured and fractured EDZ play a role in oxygen consumption. However, contrarily to scenario 1, oxygen depletion is only supported by pyrite oxidation. There is no oxygen gas penetration up to the C-steel components. Right at the entrance of the cell, the amount of goethite is quantitatively equivalent to that calculated in scenario 1, but quickly decreases along the cell length (Fig. 8D). As also observed in scenario 1, the rate of goethite precipitation quickly becomes constant with time. Deeper inside the cell, the situation is very different. There is an early precipitation of goethite (during the first year, Fig. 8C) due to the reaction of the entrapped oxygen with C-steel according to an oxic corrosion scheme but, once oxygen has been fully depleted, the chemical system turns into strongly reducing conditions. Pyrite is stable and the anoxic corrosion of steel proceeds at a constant rate, leading to cumulative magnetite precipitation over the whole lining. The effective ratio calculated between the oxic corrosion rate and the anoxic corrosion rate of the C-steel depends on the local dissolved oxygen concentration (Eq. 14), and varies from about 8 times higher at the back of the disposal cell to 20 times higher at the front.

[FIGURES 7 & 8]

4.3. Production and diffusion of hydrogen

In the water-saturation scenario 2, there is a concurrent existence of an oxidizing zone at the entrance of the disposal cell and a strongly reducing zone in the waste package zone (Fig. 5). The oxidizing zone corresponds to the presence of oxygen gas, whose partial pressure profile (Fig. 9) mostly overlaps with the dissolved oxygen profile (Fig. 5). The anoxic corrosion of C-steel materials yields to hydrogen production according to Eq. 13. As specified in Sec. 2.3, hydrogen was decoupled from any redox reactions and passively allowed to diffuse in the aqueous and gaseous phases. It is worth noting that hydrogen is a poorly soluble gas and that a large fraction goes into the gas phase once released in water.

As shown in Fig. 9, the diffusion of hydrogen gas is restricted to the unsaturated zones along the disposal cell whereas dissolved hydrogen migrates over the whole domain and, in particular, inside the argillite rock. Unlike oxygen gas, the partial pressure of hydrogen is not in a steady state and, contrarily to Fe(II), its concentration is not limited by the precipitation of a solid phase such as magnetite. Consequently, the partial pressure of hydrogen continuously increases at the back of the disposal cell to reach 0.5 bar after 100 years. The partial pressure of hydrogen declines, however, over the first 4 meters of the cell (mean value of 0.025 bar) due to the proximity of the handling drift that evacuates hydrogen by ventilation.

[FIGURE 9]

5. Conclusions

The oxic transient in underground HLW repositories has been investigated by reactive transport modeling with gas diffusion and reactivity in a 2D cell configuration. In a closed system, there is a complete and fast consumption of the oxygen initially entrapped in the cell component voids. When oxygen is renewed by the ventilation of the handling drift, the oxic perturbation depends on the balance between the kinetics of pyrite oxidation and carbon steel corrosion on the one hand, and oxygen gas diffusion on the other hand. Two modeling scenarios have been set according to the degree of water saturation and imperfect contacts between the cell components. It has been found that the extent of the oxidizing/reducing front inside the disposal cell is strongly dependent on the gas diffusion coefficient in the partially saturated zones, and to a lesser degree to the rate of pyrite oxidation (steel corrosion seems to be secondary in this respect).

When the system stays in its initial water saturation state and/or imperfect contacts are considered (scenario 1), oxygen gas diffuses along the 20 m cell length. However, the partial oxygen pressure is below 0.01 bar at the back of the cell. In this case, the cell environment globally remains oxidizing (with an oxic corrosion of carbon steel and precipitation of goethite). When the system is under an intermediate resaturation state (scenario 2), a redox contrast occurs between the reducing conditions at the back of the disposal cell (with anoxic corrosion of C-steel, magnetite formation and H_2 production) and oxidizing conditions at the front. Such a permanent differential of redox potential along the disposal cell might enhance corrosion in the zone where the redox front takes place or deeper in the cell.

The calculated mineralogical evolution is qualitatively similar to the observations of the Tournemire borehole experiment. The paragenesis goethite/magnetite found in Tournemire can either indicate that saturated conditions prevailed before the end of the experiment or that reducing conditions can take place very locally around the steel samples. New experiments with monitoring of oxygen partial pressure are underway at Tournemire, as well as investigations on the potential role of bacteria as an additional cause of oxygen consumption. The potential effect of microbial activities on oxygen consumption (respiration) and sulfate reduction should be undertaken in further calculations to strengthen this assessment, as well as the complex and coupled effects of the temperature gradient on water resaturation, multiphase transport and chemical processes.

Acknowledgements

The constructive and detailed comments of two anonymous reviewers are gratefully acknowledged, as well as our colleague Vincent Lagneau from Mines-ParisTech (France) for the implementation of the gas phase in the reactive transport code HYTEC.

References

Aachib, M., Mbonimpa, M., Aubertin, M. (2004). Measurement and prediction of the oxygen diffusion coefficient in unsaturated media, with applications to soil cover, Water Air Soil Poll. 156, 163–193.

Andra (2005). Dossier 2005 argile – Tome Architecture and management of a geological repository, Report series.

Ben Lagha, S., Crusset, D., Mabille, I., Tran, M., Bernard, M., Sutter, E. (2007). Corrosion of iron: a study for radioactive waste canisters. J. Nucl. Mater. 362, 485–492.

Bennett, D.G., Gens, R. (2008). Overview of European concepts for high-level waste and spent fuel disposal with special reference waste container corrosion. J. Nucl. Mater. 379, 1–8.

Bossart, P., Meier, P. M., Moeri, A., Trick, T., Mayor, J. C. (2002). Geological and hydraulic characterisation of the excavation disturbed zone in the Opalinus Clay of the Mont Terri Rock Laboratory. Eng. Geol. 2040, 19–38.

Charpentier, D., Cathelineau, M., Mosser-Ruck, R., Bruno, G. (2001). Evolution minéralogique des argilites en zone sous-saturée oxydée : exemple des parois du tunnel de Tournemire (Aveyron, France). C. R. Acad. Sc. Paris, Sc. Terre 332, 601–607.

Chautard, C., Lartigue, J.E., Libert, M., Marsal,F., De Windt L. (2012). An integrated experiment coupling iron/argillite interactions with bacterial activity, Proc. Chemistr. 7, 641–646.

De Craen, M., Van Geet, M., Honty, M., Weetjens, E., Sillen, X. (2008). Extent of oxidation in Boom Clay as a result of excavation and ventilation of the HADES URF: Experimental and modelling assessments. Phys. Chem. Earth 33, 350–362.

Deniau, I., Devol-Brown, I., Derenne, S., Behar, F., Largeau, C. (2008). Comparison of the bulk geochemical features and thermal reactivity of kerogens from Mol (Boom Clay), Bure (Callovo–Oxfordian argillite) and Tournemire (Toarcian shales) underground research laboratories. Sc. Total Environ. 389, 475–485.

Domènech, C., de Pablo, J., Ayora, C. (2002). Oxidative dissolution of pyritic sludge from the Aznalcollar mine (SW Spain). Chem. Geol. 190, 339–353.

Féron, D., Crusset, D., Gras, J.-M. (2008). Corrosion issues in nuclear waste disposal. J. Nucl. Mater. 379, 16–23.

Foct, F., Cabera, J., Dridi, J., Savoye, S. (2004). Prediction of long term corrosion behaviour in nuclear waste systems, Sc. Techn. series, Proc. of Workshop EUROCORR, Nice (France), 68–77.

Gaudin, A., Gaboreau, S., Tinseau, E., Bartier, D., Petit, S., Grauby, O., Foct, F., Beaufort, D. (2009). Mineralogical reactions in the Tournemire argillite after in-situ interaction with steels. Appl. Clay Sc. 43, 196–207.

Hollings, P., Hendry, M., Nicholson, N., Kirkland, R. (2001). Quantification of oxygen consumption and sulphate release rates for waste rock piles using kinetic cells: Cluff lake uranium mine, northern Saskatchewan, Canada. Appl. Geoch. 16, 1215–1230.

Jerz, J.K., Rimstidt, J.D. (2004). Pyrite oxidation in moist air, Geochim. Cosmoch. Acta 68, 701–714.

JNC (2000). H12: Project to establish the scientific and technical basis for HLW disposal in Japan. Japan Nuclear Cycle Development Institute, Supporting Report 2, Repository Design and Engineering Technology.

Johnson, L., King, F. (2008). The effect of the evolution of environmental conditions on the corrosion evolutionary path in a repository for spent fuel and high-level waste in Opalinus Clay. J. Nucl. Mater. 379, 9–15.

Kolar, M. and King, F. (1996). Modelling the consumption of oxygen by container corrosion and reaction with Fe(II). Mater. Res. Soc. Symp. Proc. 412, 547–554.

Lowson, R.T., Comarmond, M.C.J., Rajaratnam, G., Brown, P.L. (2005). The kinetics of the dissolution of chlorite as a function of pH and at 25°C. Geochim. Cosmochim. Ac. 69, 1687–1699.

Marty, N.C.M., Tournassat, C., Burnol, A., Giffaut, E., Gaucher, E.C. (2009). Influence of reaction kinetics and mesh refinement on the numerical modelling of concrete/clay interactions, J. Hydrol. 364, 58–72.

Marty, N.C.M., Fritz, B., Clément, A., Michau, N. (2010). Modelling the long term alteration of the engineered bentonite barrier in an underground radioactive waste repository. Appl. Clay Sc. 47, 82–90.

Mathieu, R., Pagel, M., Clauer, N., De Windt, L., Cabrera, Boisson, J.-Y. (2000). Paleofluid circulations records in shales : a mineralogical and geochemical study of calcite veins from the experimental Tournemire tunnel site. Eur. J. Mineral. 12, 377–390.

Matray, J.M., Savoye, S., Cabrera, J. (2007). Desaturation and structure relationships around drifts excavated in the well-compacted Tournemire's argillite (Aveyron, France), Engineer. Geol. 90, 1–16.

Molson, J., Aubertin, M., Bussière, B., Benzaazoua, M. (2005). Geochemical transport modelling of drainage from experimental mine tailings cells covered by capillary barriers, Appl. Geochem. 23, 1–24.

Moses, C.O., Herman, J.S. (1991). Pyrite oxidation at circumneutral pH. Geochim. Cosmochimi. Ac. 55, 471–482.

Motellier, S., Devol-Brown, I., Savoye, S., Thoby, D., Alberto, J.-C. (2007). Evaluation of tritiated water diffusion through the Toarcian clayey formation of the Tournemire experimental site (France), J. Contam. Hydr. 94, 99–108.

NAGRA (2002). Project Opalinus Clay, Safety Report, Demonstration of disposal feasibility for spent fuel, vitrified high-level waste and long-lived intermediate-level waste (Entsorgungsnachweis). Nagra Technical Report NTB 02-05, Nagra, Wettingen (Switzerland).

Wersin, P., Spahiu K., Bruno, J. (1994). Time evolution of dissolved oxygen and redox conditions in a HLW repository. SKB Techn. Report TR-94-02, Stockholm (Sweden).

Wersin, P., 2003. Geochemical modelling of bentonite porewater in high-level waste repositories. Journal of Contaminant Hydrology 61, 405-422.

Wersin, P., Johnson, L., Schwyn, B., Berner, U., Curti, E. (2003). Redox conditions in the near field of a repository for SF/HLW and ILW in Opalinus Clay. Rapport Technique 02-13, NAGRA, Wettingen (Switzerland).

Wolery, T. (1992). EQ3/6. A software package for geochemical modelling of aqueous systems: package overview and installation guide (version 7.0). Technical Report UCRL-MA-110662 PT I ed., Lawrence Livermore National Laboratory, USA.

Yang, C., Samper, J., Molinero, J., Bonilla, M. (2007). Modelling geochemical and microbial consumption of dissolved oxygen after backfilling a high level radioactive waste repository. J. Contam. Hydr. 93, 130–148.

Table 1.

Hydrodynamic parameters of the materials and volumetric gas/water fractions according to the water saturation degree (scenario 1: initial conditions are kept constant plus residual voids, scenario 2: almost resaturated state without residual voids).

Zones	ω [-]	$D_{e,sat}^{w}$ [$m^2.s^{-1}$]	Scenario	S^w [-]	θ^w [-]	θ^g [-]	D_e^{g} [a] [$m^2.s^{-1}$]
Argillite	0.15	1.5×10^{-11}	scenarios 1&2	1	0.15	0	0
EDZ – fissured	0.15	1.5×10^{-11}	scenario 1	0.85	0.13	0.02	1.0×10^{-9}
			scenario 2	1	0.15	0	0
EDZ – Fractured [b]	0.20	2.0×10^{-10}	scenario 1	0.25[c]	0.05	0.15	1.0×10^{-6}
			scenario 2	0.75[c]	0.15	0.05	2.5×10^{-8}
Compacted argillite (borehole)	0.40	4.0×10^{-10}	scenario 1	0.50[c]	0.20	0.20	6.0×10^{-7}
			scenario 2	0.75[c]	0.30	0.10	6.0×10^{-8}
HLW cell seal	0.36	1.5×10^{-10}	scenarios 1&2	0.80	0.29	0.07	2.5×10^{-8}

[a] The effective diffusion in the gas phase is calculated according to Eq. 4 with $D_0^g = 2\times10^{-5}$ $m^2.s^{-1}$. [b] The parameters of the zone corresponding to the carbon steel lining are identical to those of the EDZ-Fractured zone. [c] These low S^w values do not correspond to the argillite matrix only, but also take into account some cracks and voids assumed to be fully desaturated.

Table 2.

The EQ3/6 thermodynamic database has been used for the modeling, though only a subset of data were selected for dissolved redox species, gas and minerals.

Species	Reaction of formation (mass balance equation)	Log K (25 °C)
Aqueous (redox)		
Fe^{3+}/Fe^{2+}	$Fe^{3+} + 0.5\ H_2O(aq) \rightarrow Fe^{2+} + 0.25\ O_2(aq) + H^+$	-8.490
SO_4^{2-}/HS^-	$SO_4^{2-} + H^+ \rightarrow HS^- + O_2(aq)$	-138.317
Gas		
$CO_2(g)$	$CO_2(aq) \rightarrow CO_2(g)$	1.469
$H_2(g)$	$H_2(aq) \rightarrow H_2(g)$	3.105
$H_2S(g)$	$H_2S(aq) \rightarrow H_2S(g)$	0.988
$O_2(g)$	$O_2(aq) \rightarrow O_2(g)$	2.898
Solid phase		
Calcite	$Ca^{2+} + HCO_3^- \rightarrow CaCO_3(s) + H^+$	-1.849
Fe(metal)	$Fe^{2+} + H_2(aq) \rightarrow Fe(s) + 2\ H^+$	*-500[a]*
Goethite	$Fe^{3+} + 2\ H_2O(aq) \rightarrow FeOOH(s) + 3\ H^+$	-0.535
Gypsum	$Ca^{2+} + SO_4^{2-} + H_2O(aq) \rightarrow CaSO_4{:}H_2O(s) + H^+$	4.482
Magnetite	$Fe^{2+} + 2\ Fe^{3+} + 4\ H_2O(aq) \rightarrow Fe_3O_4(s) + 8\ H^+$	-10.472
Melanterite	$Fe^{2+} + SO_4^{2-} \rightarrow FeSO_4{:}7H_2O(s)$	2.349
Pyrite	$Fe^{2+} + 0.25\ SO_4^{2-} + 1.75\ HS^- + 0.25\ H^+ \rightarrow FeS_2(s) + H_2O(aq)$	24.653
Quartz	$SiO_2(aq) \rightarrow SiO_2(s)$	3.999
Siderite	$Fe^{2+} + HCO_3^- \rightarrow FeCO_3(s) + H^+$	0.192

[a] Arbitrary value fixed to keep the corrosion of metallic iron under a full kinetic control.

Table 3.

Stoichiometry, constants, cationic exchange capacity (CEC) and site densities for the cation exchange and surface complexation reactions (Wersin, 2003).

Reaction	log*K* (25 °C)	
Cation exchange [a]		
$K^+ + \overline{Na} \rightarrow \overline{K} + Na^+$	0.60	
$Ca^{2+} + 2\ \overline{Na} \rightarrow \overline{Ca} + 2\ Na^+$	0.41	
CEC		15 meq/100g (argillite) 75 meq/100g (MX 80)
Surface complexation [b]		
$S_1\text{-}OH + H^+ \rightarrow S_1\text{-}OH_2^+$	4.5	
$S_1\text{-}OH \rightarrow S_1\text{-}O^- + H^+$	-7.9	
$S_2\text{-}OH + H^+ \rightarrow S_2\text{-}OH_2^+$	6.0	
$S_2\text{-}OH \rightarrow S_2\text{-}O^- + H^+$	-10.5	
Site density S_1-OH		1.25 μmol.m^{-2}
S_2-OH		1.25 μmol.m^{-2}

[a] Gaines-Thomas formalism; [b] double layer model.

Table 4.

Kinetics parameters for pyrite dissolution/precipitation and steel corrosion under oxic (*ox*) and anoxic (*anox*) conditions at 25 °C (See text, Eq. 11).

Parameters	Units	Pyrite	Carbon steel liner
k_{ox}	[mol.m^{-2}.s^{-1}]	5×10^{-9}	3×10^{-5} [a]
		5×10^{-8} [b]	*3×10^{-6} [c]*
$k_{ox}(O_2^{init}(aq))^{0.5}$	[mol.m^{-2}.s^{-1}]	8×10^{-11} [d]	5×10^{-7} [a,d]
		8×10^{-10} [b,d]	*5×10^{-8} [c,d]*
k_{anox}	[mol.m^{-2}.s^{-1}]	1×10^{-16}	1×10^{-8} [e]
f_{Sw}	[-]	1.0	1.0
		0.2 (only for EDZ-Fractured in scenario 1)	0.2 (only in scenario 1)
A_s	[m^2.g^{-1}]	1×10^{-1}	2×10^{-6}

[a] Global rate constant including general and pitting corrosions under oxic conditions, 5×10^{-7} mol.m^{-2}.s^{-1} ~ 100 um.y^{-1}; [b] sensitivity analysis, higher range of the rate constants found in literature; [c] sensitivity analysis, without pitting corrosion; [d] assuming an initial dissolved oxygen activity of 2.5×10^{-4} (25 °C, atmospheric conditions); [e] 1.0×10^{-8} mol.m^{-2}.s^{-1} ~ 2 um.y^{-1}.

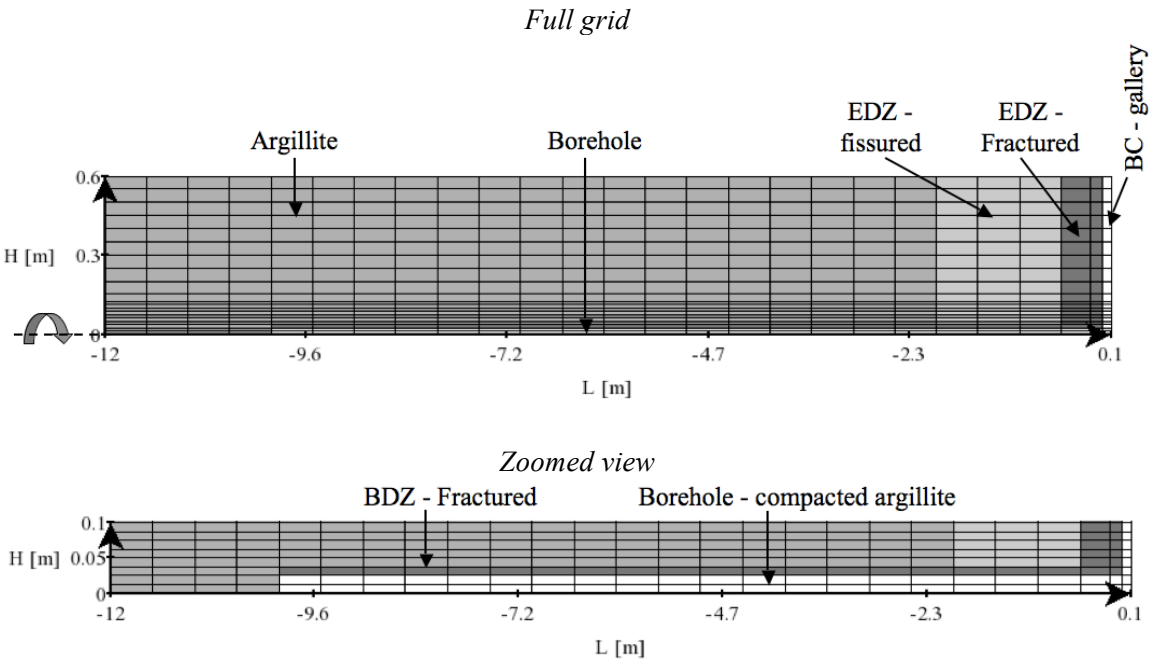

Figure 1. Tournemire borehole: 2D-cylindrical modeling grid (rotation around the length axis L); BC stands for the boundary conditions, BDZ for the damaged borehole zone and EDZ for the excavated damaged zone of the gallery.

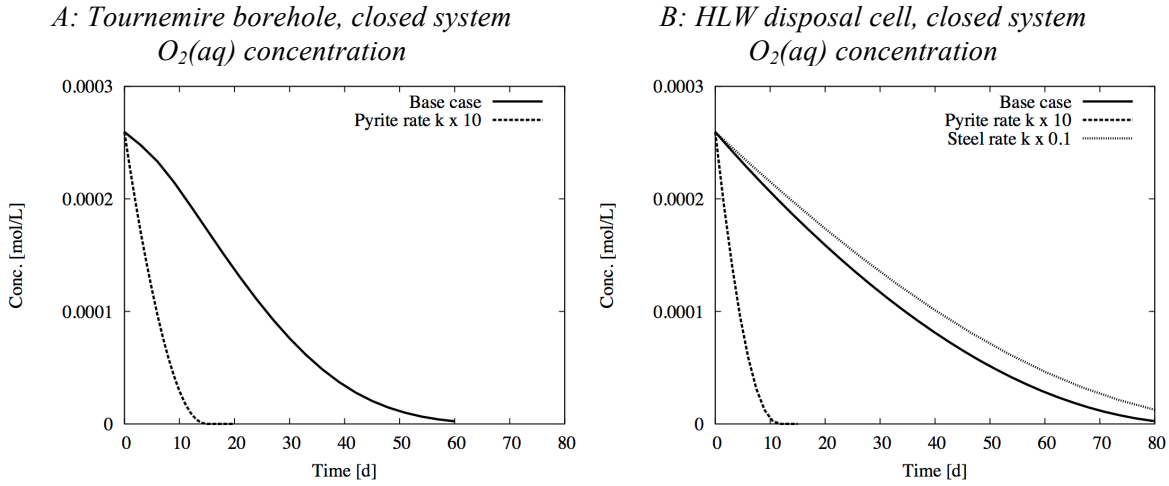

Figure 2. Dissolved oxygen consumption under water-saturation scenario 1b, i.e. a closed system without air ventilation, calculated at the back of the Tournemire borehole (-9.25, 0.02 m) and the middle of the HLW disposal cell (-15.25, 0.35 m); sensitivity analysis on the rate constant of pyrite oxidation and steel oxic corrosion.

Scenario 1 – O_2(aq) and Eh

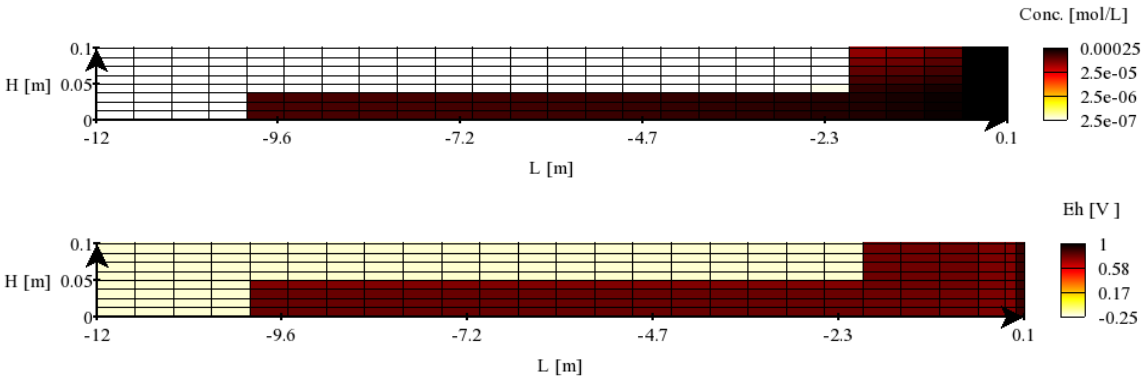

Scenario 2 – O_2(aq) and Eh

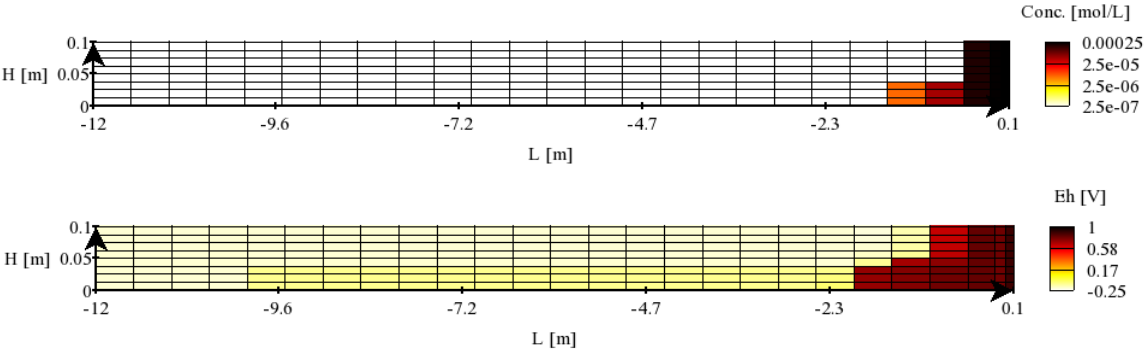

Figure 3. Tournemire borehole: steady-state 2D-profiles of dissolved oxygen and redox potential Eh.

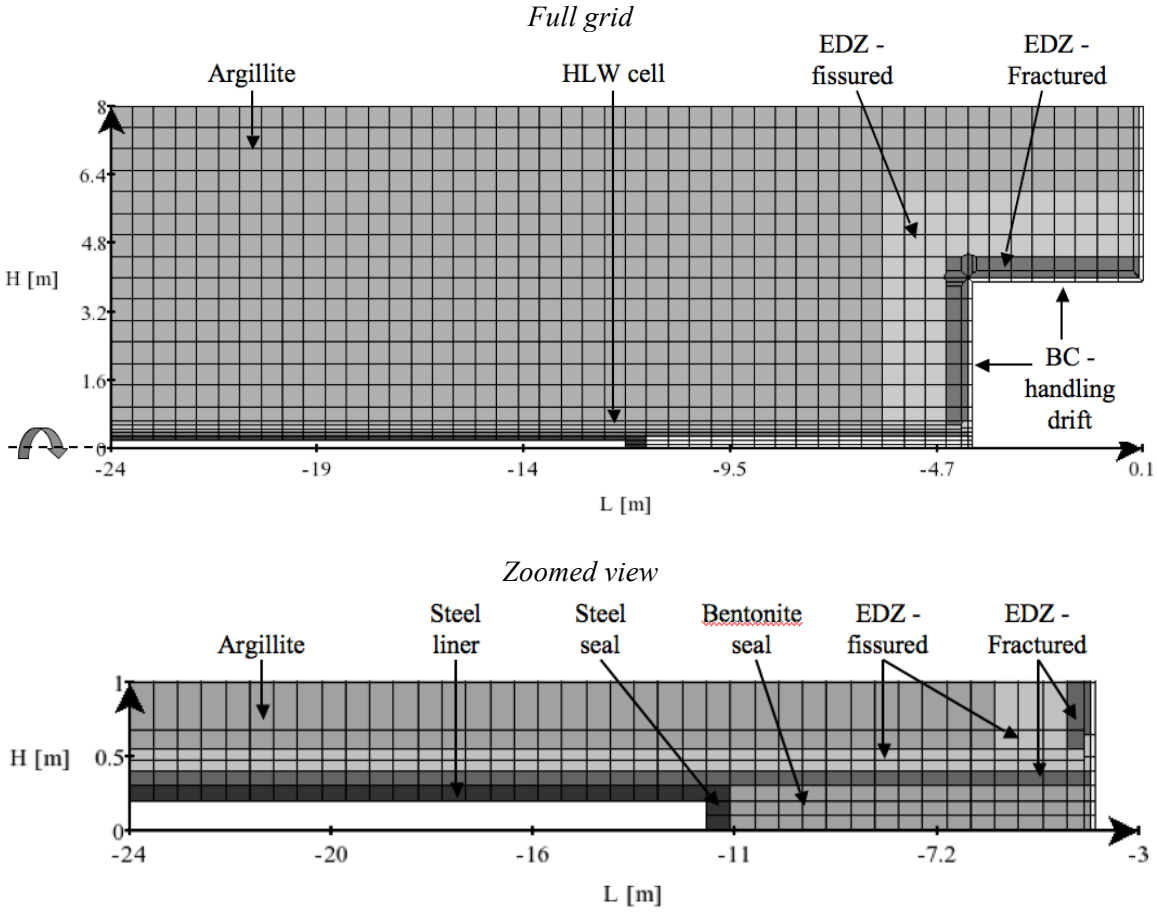

Figure 4. HLW disposal cell: 2D-cylindrical modeling grid (rotation around the length axis L); BC stands for boundary conditions, EDZ for the excavated damaged zone of the handling drift and the disposal cell.

Scenario 1 – O_2(aq) and Eh

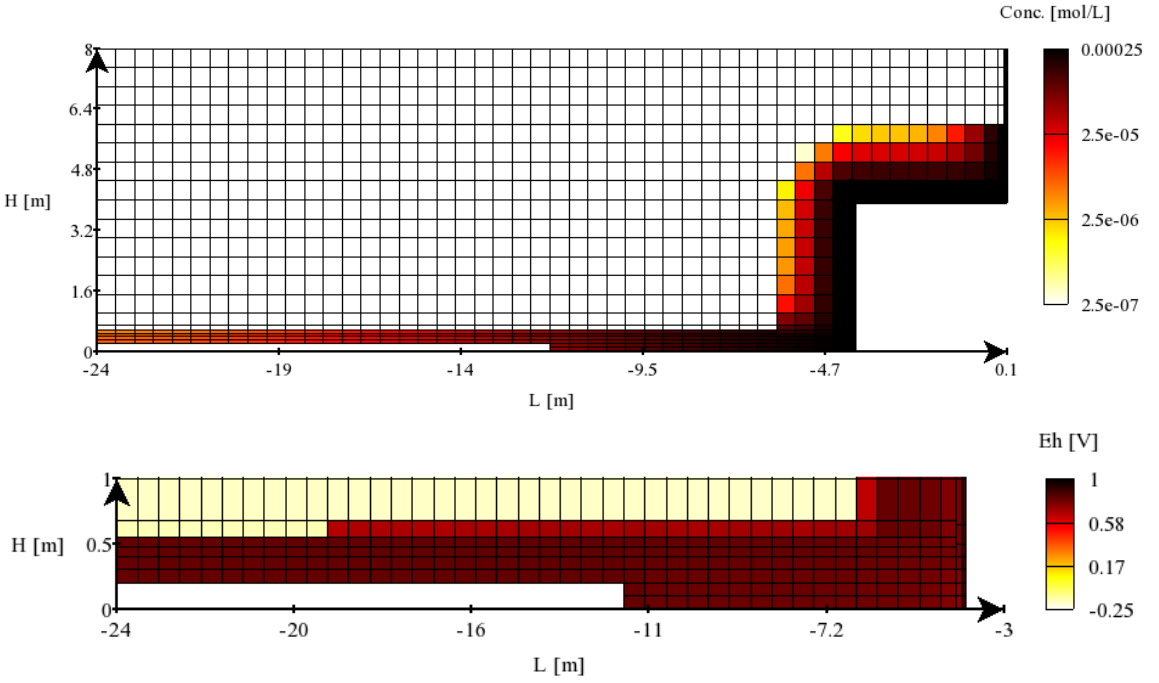

Scenario 2 – O_2(aq) and Eh

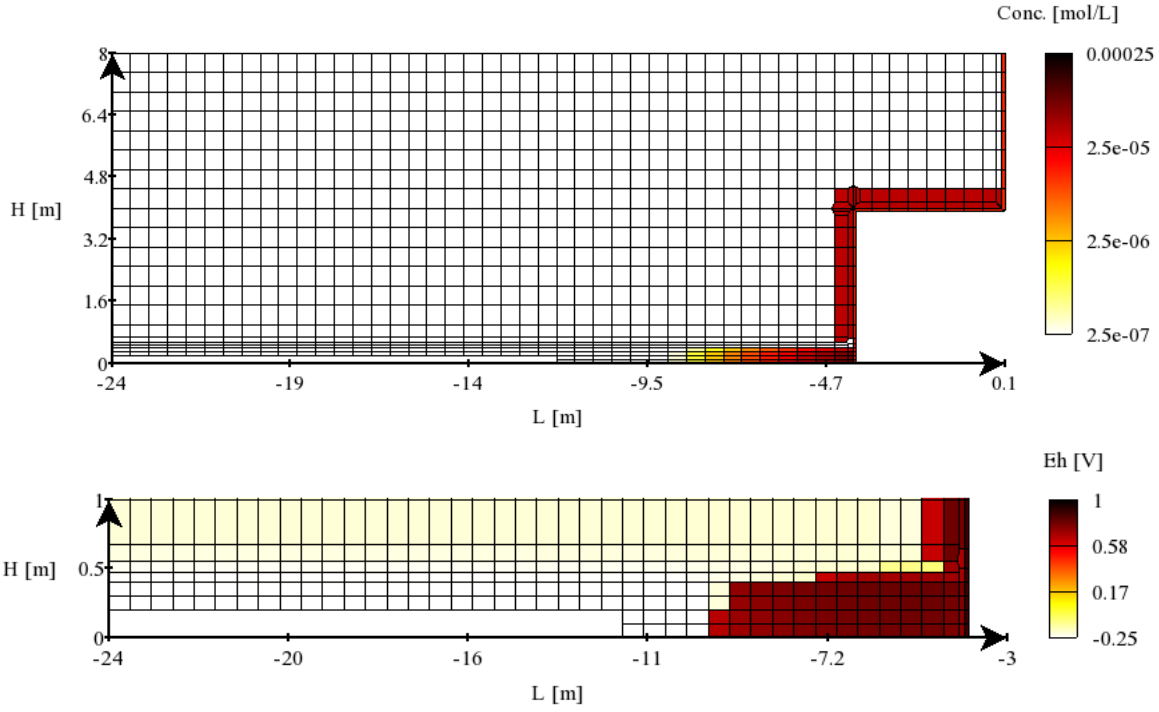

Figure 5. HLW disposal cell: steady-state 2D-profiles of dissolved oxygen and redox potential Eh.

Scenario 1 – Eh (pyrite rate ×10)

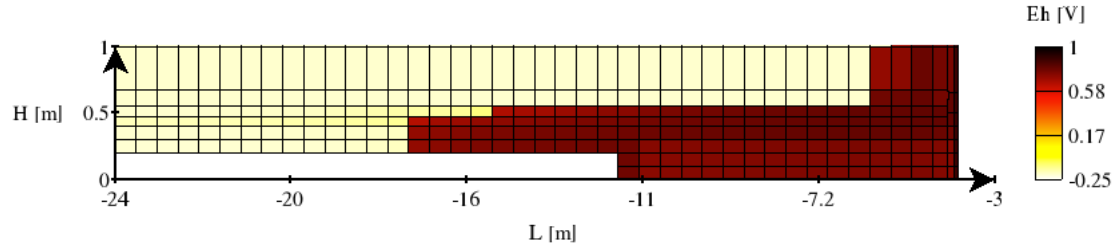

Scenario 2 – Eh (pyrite rate ×10)

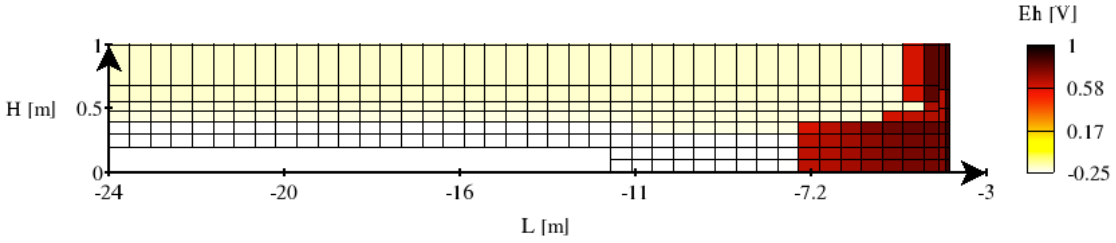

Figure 6. Same as Fig. 5 but for a rate constant of pyrite oxidation 10 times higher (sensitivity analysis): HLW disposal cell, steady-state 2D-profiles.

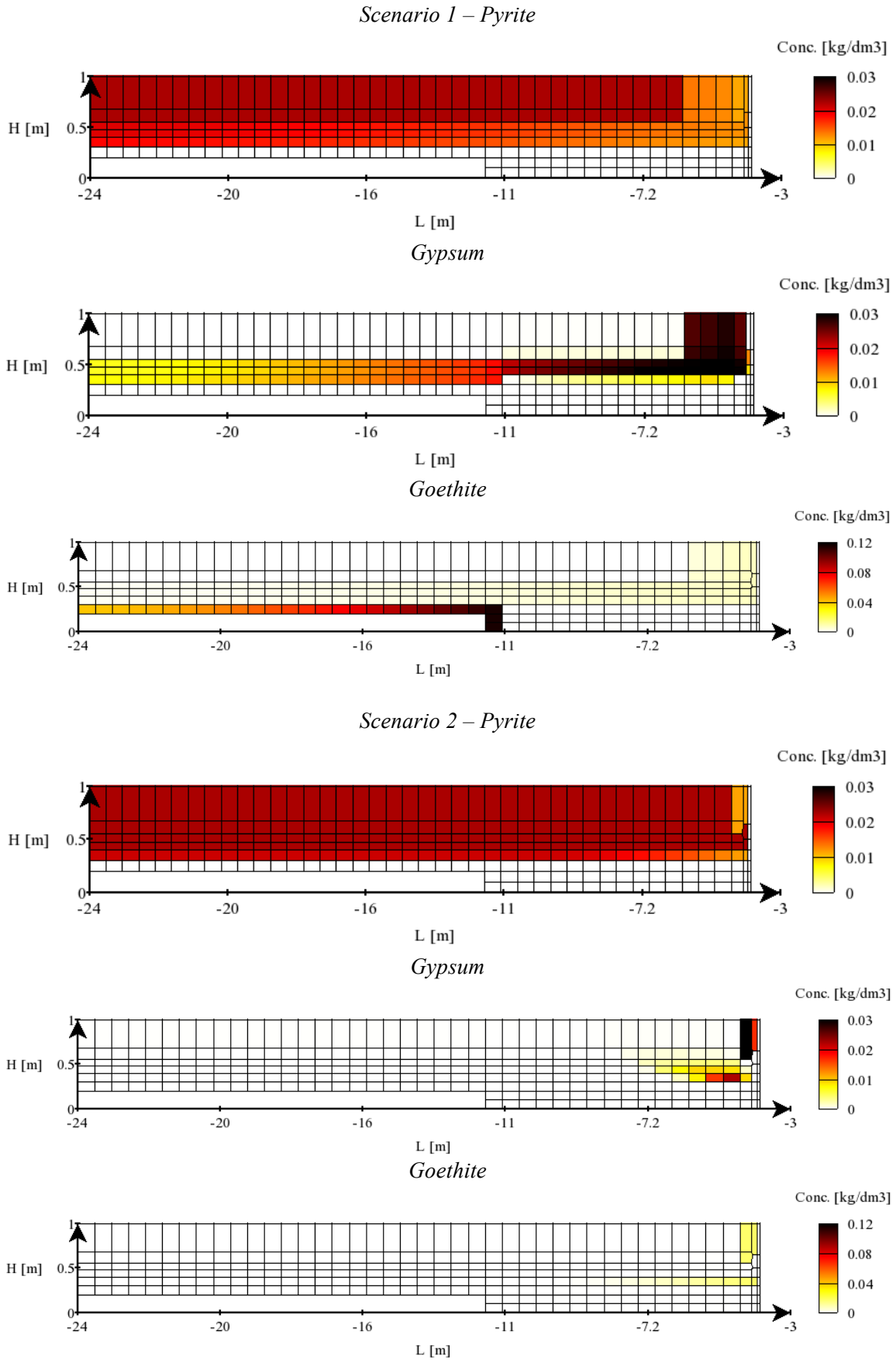

Figure 7. HLW disposal cell: 2D-profiles of pyrite, gypsum and goethite contents, calculated after 100 y.

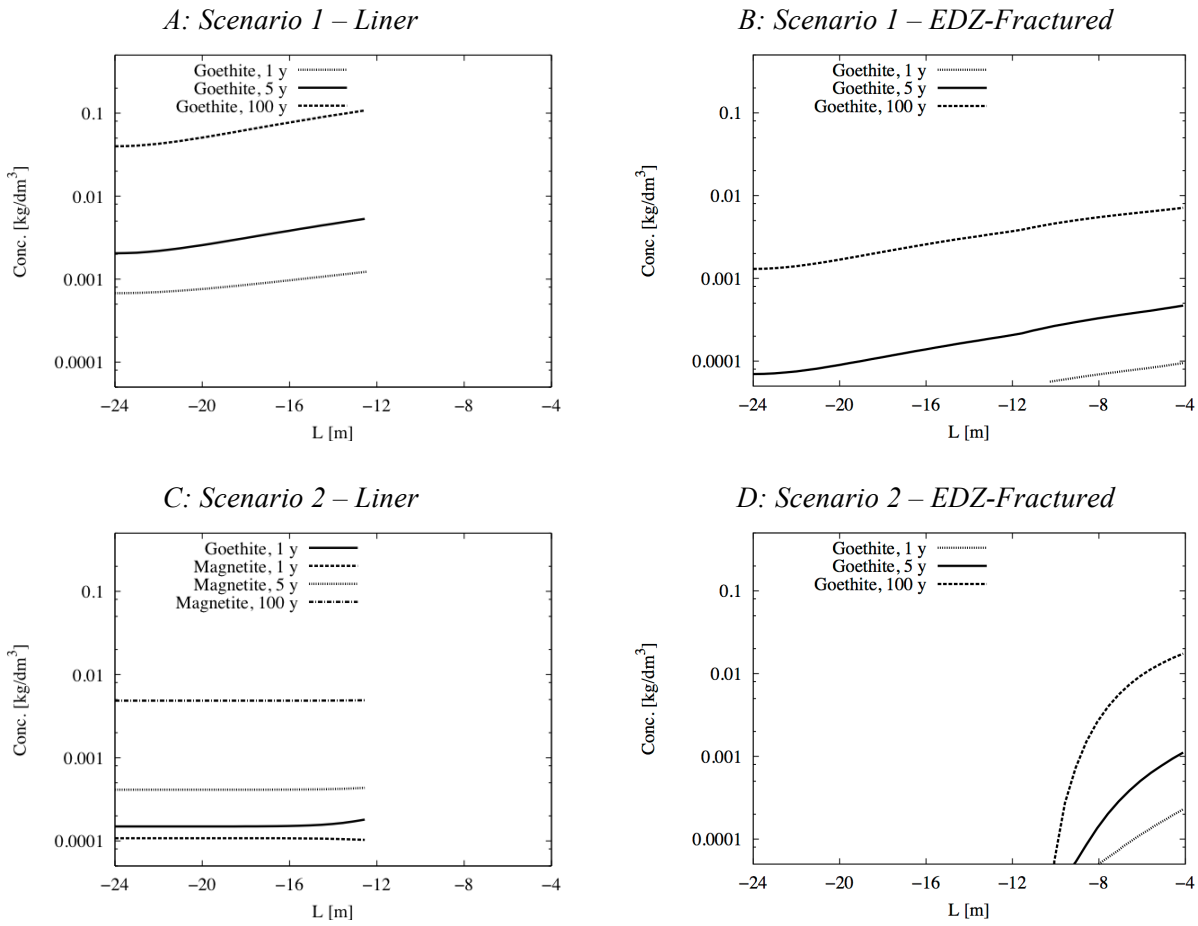

Figure 8. HLW disposal cell: longitudinal 1D-cross sections of goethite and magnetite contents calculated along the liner, from (-24, 0.25 m) to (-4.1, 0.25 m), and the fractured EDZ, from (-24, 0.35 m) to (-4.1, 0.35 m).

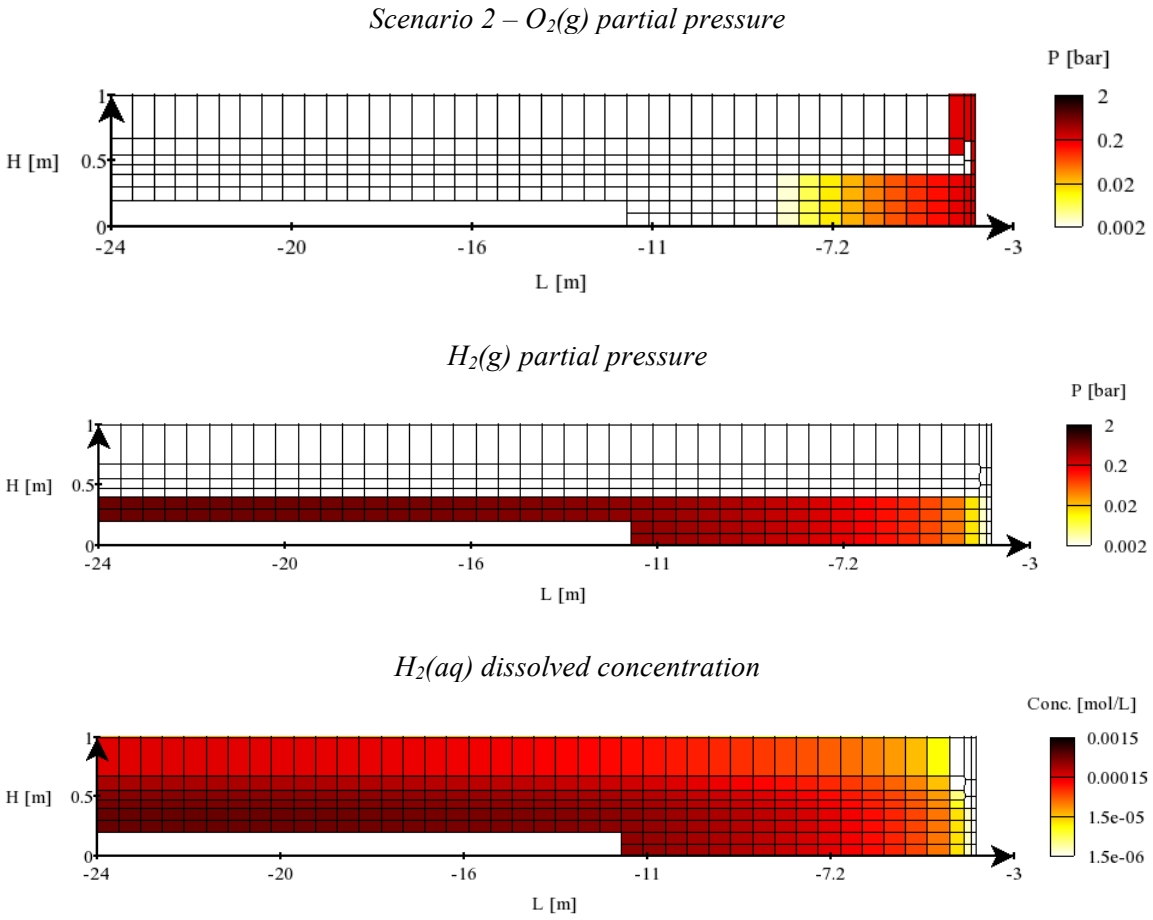

Figure 9. HLW disposal cell: 2D-profiles of oxygen and hydrogen partial pressures and of dissolved hydrogen concentration, calculated after 100 y for scenario 2.